The Astrophysical Journal, 799:96 (13pp), 2015 January 20 doi:10.1088/0004-637X/799/1/96

DUST CONTINUUM EMISSION AS A TRACER OF GAS MASS IN GALAXIES

Brent A. Groves[1], Eva Schinnerer[1], Adam Leroy[2], Maud Galametz[3], Fabian Walter[1], Alberto Bolatto[4], Leslie Hunt[5], Daniel Dale[6], Daniela Calzetti[7], Kevin Croxall[8], and Robert Kennicutt Jr.[9]
[1] Max Planck Institute for Astronomy, Königstuhl 17, D-69117 Heidelberg, Germany; brent@mpia.de
[2] National Radio Astronomy Observatory, 520 Edgemont Road, Charlottesville, VA 22903, USA
[3] ESO, Karl-Schwarzschild Str. 2, D-85748 Garching, Germany
[4] Department of Astronomy, University of Maryland, College Park, MD 20742, USA
[5] INAF-Osservatorio Astrofisico di Arcetri, Largo E. Fermi 5, I-50125 Firenze, Italy
[6] Department of Physics and Astronomy, University of Wyoming, Laramie, WY 82071, USA
[7] Department of Astronomy, University of Massachusetts, Amherst, MA 01003, USA
[8] Department of Astronomy, The Ohio State University, 4051 McPherson Laboratory, 140 West 18th Avenue, Columbus, OH 43210, USA
[9] Institute of Astronomy, University of Cambridge, Madingley Road, Cambridge CB3 0HA, UK
Received 2014 May 16; accepted 2014 October 16; published 2015 January 20

ABSTRACT

We use a sample of 36 galaxies from the KINGFISH (*Herschel* IR), HERACLES (IRAM CO), and THINGS (Very Large Array H I) surveys to study empirical relations between *Herschel* infrared (IR) luminosities and the total mass of the interstellar gas (H_2 + H I). Such a comparison provides a simple empirical relationship without introducing the uncertainty of dust model fitting. We find tight correlations, and provide fits to these relations, between *Herschel* luminosities and the total gas mass integrated over entire galaxies, with the tightest, almost linear, correlation found for the longest wavelength data (SPIRE 500). However, we find that accounting for the gas-phase metallicity (affecting the dust to gas ratio) is crucial when applying these relations to low-mass, and presumably high-redshift, galaxies. The molecular (H_2) gas mass is found to be better correlated with the peak of the IR emission (e.g., PACS160), driven mostly by the correlation of stellar mass and mean dust temperature. When examining these relations as a function of galactocentric radius, we find the same correlations, albeit with a larger scatter, up to a radius of $r \sim 0.7\, r_{25}$ (containing most of a galaxy's baryonic mass). However, beyond that radius, the same correlations no longer hold, with increasing gas (predominantly H I) mass relative to the infrared emission. The tight relations found for the bulk of the galaxy's baryonic content suggest that total gas masses of disk-like (non-merging/ULIRG) galaxies can be inferred from far-infrared continuum measurements in situations where only the latter are available, e.g., in ALMA continuum observations of high-redshift galaxies.

Key words: galaxies: ISM – infrared: galaxies

Supporting material: figure sets

1. INTRODUCTION

Two of the fundamental parameters driving the evolution of galaxies across cosmic time is their total gas mass, and gas-mass surface density. The total gas mass of galaxies limits the total amount of stars that can form in a galaxy at any time, while its surface density is directly linked with the rate of star formation via the observed Kennicutt–Schmidt relation (K-S relation; e.g., Kennicutt 1998; Leroy et al. 2013b). The increase of the cosmic star formation rate (SFR) density up to redshifts of three to four (e.g., Karim et al. 2011) is theorized to be caused by the increase in the cosmic gas-mass density (and therefore the average total gas mass of galaxies) with increasing redshift (as suggested by, e.g., Obreschkow & Rawlings 2009). However, directly measuring the gas-mass density out to these redshifts is a difficult task.

Existing large area surveys of the 21 cm H I fine-structure line that traces the atomic gas have only measured the local universe ($z \lesssim 0.05$, e.g., HIPASS, Barnes et al. 2001, and ALFALFA, Haynes et al. 2011). In the near future, deeper surveys with the precursors for the Square Kilometer Array (SKA) such as DINGO (Meyer 2009) on the Australian SKA Pathfinder will reach at most $z \sim 0.4$ (Duffy et al. 2012). However, it will not be until SKA is available that H I will be observed in emission at $z > 1$, and even then it is expected to reach at most $z \sim 1.5$ (Abdalla & Rawlings 2005). This leaves only H I absorption line studies, such as damped Lyα systems (e.g., Prochaska et al. 2005), as the only determination of the evolution of the H I mass function over cosmic time.

For molecular gas, surveys of large numbers of galaxies have been limited due to the difficulty of observing the transitions from the CO molecule in the (sub)millimeter. The two largest efforts have been the FCRAO Extragalactic CO Survey (Young et al. 1995), which measured the CO(1–0) line in 300 nearby galaxies, and the COLD GASS survey (Saintonge et al. 2011a, 2011b), which measured fluxes in the CO(1–0) line for a purely mass-selected sample of ∼350 galaxies at $0.025 < z < 0.05$, matched in *Galaxy Evolution Explorer*, Arecibo, and Sloan Digital Sky Survey (SDSS) imaging. The FCRAO sample has recently been extended with CO(1–0) observations of a further 59 nearby galaxies as part of the *Herschel* Reference Survey (Boselli et al. 2014a, 2014b). At higher redshift, the CO lines are still observable, but samples are smaller in number. While molecular gas measures were originally limited to very luminous, rare objects (e.g., Solomon & Vanden Bout 2005), more typical galaxies are now being observed out to $z \sim 0.5$ (e.g., EGNoG; Bauermeister et al. 2013), and farther out to $z \sim$ 2–3 (e.g., PHIBSS; Tacconi et al. 2013), with a full review of these surveys available in Carilli & Walter (2013). With ALMA now operating, the samples of high-redshift galaxy molecular gas masses will only increase. However, given its small instantaneous field of view, ALMA is a relatively slow survey instrument, and, while already providing impressive targeted observations, will not be suitable for very wide area

blind CO surveys at $z \sim 2$–3 (Obreschkow & Rawlings 2009), though smaller blind searches have already been carried out in smaller regions (e.g., Decarli et al. 2014; Walter et al. 2014).

Another potential tracer of the total gas mass is the infrared emission arising from dust. The amount of dust has long been known to be associated with a gas column within the Milky Way (e.g., Jenkins & Savage 1974), and dust extinction has been used to map gas columns at higher dynamic ranges and spatial resolution than available from gas emission lines (e.g., Lada et al. 1994; Kainulainen et al. 2011). However, in extragalactic studies, the lower physical resolution mixes lines of sight, making internal extinction a poor tracer of the gas column (e.g., Kreckel et al. 2013, see also Boquien et al. 2013), and relying on the rare occultation of relatively bright background sources is not feasible for large extragalactic studies. However, the dust continuum emission in the infrared—submillimeter range is a direct tracer of the total dust opacity and, if a mean grain emissivity is assumed, the dust column.

The idea of using the submillimeter continuum emission to measure the mass of the interstellar medium (ISM) has existed for a while, having been suggested by Hildebrand 1983 and used by Guelin et al. (1993, 1995) in nearby galaxies. As an independent tracer of the gas mass, the dust continuum has also been directly compared with CO observations in nearby galaxies to constrain the conversion factor between CO and gas mass (i.e., the "*X*" factor, Israel 1997, Boselli et al. 2002, Magrini et al. 2011, Sandstrom et al. 2013, and the review by Bolatto et al. 2013). Direct comparisons of the submillimeter continuum and gas content in galaxies have also been explored in Corbelli et al. (2012), Eales et al. (2012), and Scoville et al. (2014), and this correlation has already been used to estimate the total gas masses in higher redshift galaxies by Magdis et al. (2012) and Scoville et al. (2014).

However, the dust continuum emission is not a simple direct tracer of the gas mass. The dust emission is dependent upon the temperature of the dust grains, the conversion to dust column depends upon knowledge of the grain emissivity, and finally, the conversion of the dust column to gas mass depends upon the dust to gas ratio (DGR). Modeling the IR spectral energy distribution (SED) typically involves the use of both physically based models for the dust grains and reasonable assumptions for the heating of the grains to determine the total dust column directly from the IR emission (see, e.g., Draine & Li 2007). This approach has obtained reasonable results in many nearby galaxies (e.g., Draine et al. 2007; Aniano et al. 2012; Compiègne et al. 2011). However, systematic uncertainties lie in both the dust models and the assumptions on the heating radiation field (and the parameters in each), as well as the fitting procedure itself, introducing another level of complexity in determining the interstellar gas mass. The recent work of Eales et al. (2012) demonstrated that using a simple modified-blackbody model for the dust emission and a constant conversion factor from dust to gas are not unreasonable assumptions for the determination of total gas mass. They found a good correlation of the *Herschel*-based dust masses with total gas masses determined from H I and CO data in 10 nearby galaxies, with an estimated 25% error on the dust method. However, systematic uncertainties were found to dominate this method as well, with Eales et al. (2012) demonstrating the sensitivity of the determined dust mass to the fitted dust temperature, and the sensitivity of this dust temperature to both the assumed emissivity (as demonstrated in detail in Shetty et al. 2009) and the observed wavelengths fitted.

We can bypass these systematic issues by directly comparing the far-IR to submillimeter continuum emission to the various tracers of the gas phases directly. We can then determine calibrations linking the monochromatic IR emission and gas tracers by exploring a wide range of objects, which also enable the exploration of dependencies on other physical parameters like gas-phase metallicity. A direct comparison of the submillimeter emission with gas tracers has already been explored somewhat by Bourne et al. (2013), who used a sample of 20 galaxies within the *Herschel*-ATLAS survey with existing H I and new CO data. They found that the submillimeter fluxes appear to be strongly associated with the diffuse atomic and molecular gas phases, and that the FIR/CO luminosity ratio decreases with increasing luminosity. However, even though several IR fluxes were explored, the range in the submillimeter luminosities of the galaxies was small. The most detailed examination to date has been by Scoville et al. (2014), who used both local luminous IR galaxies and higher redshift submillimeter galaxies with 850 μm fluxes to calibrate the ratio of submillimeter luminosity to the ISM mass assuming a constant emissivity to mass ratio. They found that the ISM mass and 850 μm luminosity correlated within a factor of two for their galaxy sample, and then used this correlation to determine the ISM masses in stacked submillimeter ALMA observations of high-redshift galaxies. However, their analysis was focused on more luminous sources and may not hold for all galaxies.

To improve upon these surveys, we use the most comprehensive nearby galaxy surveys available: the KINGFISH (Kennicutt et al. 2011), THINGS (Walter et al. 2008), and HERACLES (Leroy et al. 2009) surveys for the IR, H I, and CO data, respectively. The galaxies in these surveys cover a wide range in metallicity, stellar mass, and SFRs, and with all these parameters measured in a consistent manner from the associated ancillary data sets. It thus represents one of the largest homogenous data sets for CO and H I in nearby galaxies, and covers the full IR SED from 70 to 500 μm. In addition, the galaxies in the sample are near enough that they can be resolved, and radial trends can be examined as well. This enables us to determine the correlation of submillimeter emission with gas mass over a wide range of galaxy parameters, and explore the limiting conditions where the submillimeter emission can be used. In the following section, we introduce the surveys and the galaxy sample, followed by a description of the theory in Section 3.1, and explore a direct comparison of the integrated IR emission to the total gas masses of galaxies in Section 3. We explore the issues of internal variations and radial trends in Section 4, and summarize our findings in Section 5.

2. DATA SETS

2.1. Galaxy Sample

Our galaxy sample arises from the intersection of three complementary large programs surveying nearby galaxies; KINGFISH (Kennicutt et al. 2011), THINGS (Walter et al. 2008), and HERACLES (Leroy et al. 2009). These programs provide us with tracers of both the integrated gas and dust masses of galaxies, and resolved maps down to ~kpc scales extending well beyond the optical radii for the H I and IR data. The matched data sets result in 36 galaxies, ranging from dwarf galaxies to massive spirals, with the names and galaxy properties listed in Table 1. All values were taken from Kennicutt et al. (2011), and references therein except for the metallicity, which is from Moustakas et al. (2010) when available. The sample is

Table 1
Galaxy Properties of the Matched KINGFISH-HERACLES-THINGS Sample[a]

Galaxy	R.A. (J2000)	Decl. (J2000)	Distance (Mpc)	P.A. (deg)	Major[b] (arcmin)	Minor (arcmin)	Metallicity[c] $12+\log(O/H)$	$\log M_\star$ $M_\odot$	SFR $M_\odot$ yr^{-1}
DDO053	08:34:07	+66:10:54	3.61	132	1.5	1.3	7.98	6.35	0.0060
DDO154	12:54:05	+27:08:59	4.3	50	3.0	2.2	8.02	6.63	0.0020
HoI	09:40:32	+71:10:56	3.9	0	3.6	3.0	8.04	6.87	0.0040
HoII	08:19:05	+70:43:12	3.05	15	7.9	6.3	8.13	7.59	0.036
IC2574	10:28:23	+68:24:44	3.79	56	13.2	5.4	8.23	8.2	0.057
M81dwB	10:05:31	+70:21:52	3.6	140	0.9	0.6	8.2	6.36	0.0010
NGC 337	00:59:50	−07:34:41	19.3	130	2.9	1.8	8.84	9.32	1.3
NGC 628	01:36:42	+15:47:00	7.2	25	10.5	9.5	8.88	9.56	0.68
NGC 925	02:27:17	+33:34:45	9.12	107	10.5	5.9	8.73	9.49	0.54
NGC 2146	06:18:38	+78:21:25	17.2	123	6.0	3.4	...	10.3	7.94
NGC 2798	09:17:23	+41:59:59	25.8	160	2.6	1.0	9.04	10.04	3.38
NGC 2841	09:22:03	+50:58:35	14.1	153	8.1	3.5	9.19	10.17	2.45
NGC 2976	09:47:15	+67:54:59	3.55	155	5.9	2.7	8.98	8.96	0.082
NGC 3077	10:03:19	+68:44:02	3.83	45	5.4	4.5	...	9.34	0.094
NGC 3184	10:18:17	+41:25:28	11.7	135	7.4	6.9	9.07	9.5	0.66
NGC 3198	10:19:55	+45:32:59	14.1	35	8.5	3.3	8.78	9.83	1.01
NGC 3351	10:43:58	+11:42:14	9.33	12	7.4	5.0	9.21	10.24	0.58
NGC 3521	11:05:49	−00:02:09	11.2	160	11.0	5.1	9.06	10.69	1.95
NGC 3627	11:20:15	+12:59:30	9.38	173	9.1	4.2	8.99	10.49	1.7
NGC 3938	11:52:49	+44:07:15	17.9	28	5.4	4.9	9.06	9.46	1.77
NGC 4236	12:16:42	+69:27:45	4.45	162	21.9	7.2	8.74	8.36	0.13
NGC 4254	12:18:50	+14:24:59	14.4	23	5.4	4.7	9.08	9.56	3.92
NGC 4321	12:22:55	+15:49:21	14.3	30	7.4	6.3	9.12	10.3	2.61
NGC 4536	12:34:27	+02:11:17	14.5	130	7.6	3.2	9.0	9.44	2.17
NGC 4569	12:36:50	+13:09:46	9.86	23	9.5	4.4	9.26	10.0	0.29
NGC 4579	12:37:44	+11:49:05	16.4	95	5.9	4.7	9.22	10.02	1.1
NGC 4625	12:41:53	+41:16:26	9.3	27	2.2	1.9	9.05	8.72	0.052
NGC 4631	12:42:08	+32:32:29	7.62	86	15.5	2.7	8.75	9.76	1.7
NGC 4725	12:50:27	+25:30:03	11.9	35	10.7	7.6	9.1	10.52	0.44
NGC 4736	12:50:53	+41:07:14	4.66	116	11.2	9.1	9.04	10.34	0.38
NGC 5055	13:15:49	+42:01:45	7.94	102	12.6	7.2	9.11	10.55	1.04
NGC 5457	14:03:13	+54:20:57	6.7	39	28.8	26.0	...	9.98	2.33
NGC 5474	14:05:02	+53:39:44	6.8	97	4.8	4.3	8.83	8.7	0.091
NGC 5713	14:40:12	−00:17:20	21.4	11	2.8	2.5	9.03	10.07	2.52
NGC 6946	20:34:52	+60:09:14	6.8	63	11.5	9.8	8.99	9.96	7.12
NGC 7331	22:37:04	+34:24:56	14.5	168	10.5	3.7	9.05	10.56	2.74

Notes.
[a] Values taken directly from Kennicutt et al. (2011) and the NASA Extragalactic Database.
[b] R_{25} is equal to half the major axis.
[c] Metallicity shown here is the average galaxy value from Moustakas et al. (2010) or Kennicutt et al. (2011) when unavailable, using the Kobulnicky & Kewley (2004) calibration.

dominated by spiral galaxies and irregulars. The stellar masses and SFRs both cover approximately four orders of magnitude, and approximately two orders of magnitude in specific star formation rates (sSFR = SFR/$M_\star$).

2.2. Infrared Luminosities

The infrared data we use in this work are all from the KINGFISH sample (Key Insights into Nearby Galaxies; a Far Infrared Survey with *Herschel*; Kennicutt et al. 2011), an imaging and spectroscopic survey of 61 nearby ($d < 30$ Mpc) galaxies with the *Herschel Space Observatory* (Pilbratt et al. 2010). This survey provides imaging in six IR bands; 70, 100, and 160 μm with PACS (Poglitsch et al. 2010), and 250, 350, and 500 μm with SPIRE (Griffin et al. 2010), with the observing strategy described in detail in Kennicutt et al. (2011). All bands (PACS and SPIRE) are processed from level 1 using SCANAMORPHOS v17.0 (Roussel 2012). The PACS data are calibrated using Flight Model 6, however, the 160 μm band has a uniform correction factor of 0.925 applied to it to correct for the PACS distortion flatfield not included in the original scanamorphos reduction.[10] As the effect is of the order of 1% for the other PACS bands, well below the photometric uncertainties, no correction is applied to these bands. The SPIRE bands assume factors of 97.7, 55.0, and 26.0 to convert from Jy beam^{-1} to MJy sr^{-1} for the SPIRE 250 μm, 350 μm, and 500 μm bands, respectively.

To measure the fluxes of each galaxy, we first convolve all bands to a beam size of ∼36″, the resolution of the SPIRE 500 μm beam (the lowest resolution band), using the convolution kernels of Aniano et al. (2012). We then use the galaxy centers listed in Table 1 and elliptical apertures as used by Dale et al. (2012) to determine the total integrated galaxy flux. These elliptical apertures have the same position angles and axis ratios as listed in Table 1, and encompass the full optical and IR light, and typically extend to ∼2 optical radii. The background for all images was assumed to be flat and was determined as

[10] See http://www2.iap.fr/users/roussel/herschel/ for details.

Table 2
Integrated IR Fluxes of the 36 KINGFISH Galaxies in the Six *Herschel* Bands[a]

Galaxy	PACS70 (Jy)	PACS100 (Jy)	PACS160 (Jy)	SPIRE 250 (Jy)	SPIRE 350 (Jy)	SPIRE 500 (Jy)
DDO053	0.34 ± 0.08	0.50 ± 0.10	0.31 ± 0.06	0.22 ± 0.03	0.14 ± 0.01	0.05 ± 0.01
DDO154	0.00 ± 0.07	0.49 ± 0.07	0.12 ± 0.08	0.18 ± 0.06	0.12 ± 0.03	0.05 ± 0.02
HoI	0.71 ± 0.23	0.53 ± 0.37	0.26 ± 0.18	0.44 ± 0.10	0.27 ± 0.02	0.14 ± 0.02
HoII	3.60 ± 0.67	3.53 ± 0.82	3.26 ± 0.54	1.66 ± 0.33	0.99 ± 0.22	0.51 ± 0.14
IC2574	5.56 ± 1.19	7.84 ± 0.80	8.90 ± 1.48	6.05 ± 0.75	4.34 ± 0.35	1.83 ± 0.19
M81dwB	0.09 ± 0.05	0.17 ± 0.11	0.11 ± 0.06	0.17 ± 0.01	0.10 ± 0.01	0.04 ± 0.01
NGC 337	13.44 ± 0.41	20.12 ± 0.22	18.78 ± 0.25	9.11 ± 0.37	4.09 ± 0.18	1.66 ± 0.10
NGC 628	41.07 ± 2.48	79.11 ± 2.60	111.20 ± 2.49	65.36 ± 0.93	31.55 ± 0.50	12.46 ± 0.24
NGC 925	12.75 ± 1.13	25.85 ± 0.76	35.74 ± 0.74	26.19 ± 0.61	14.58 ± 0.32	6.98 ± 0.14
NGC 2146	203.14 ± 0.53	241.89 ± 0.54	176.05 ± 0.33	66.08 ± 0.21	23.97 ± 0.14	7.75 ± 0.09
NGC 2798	25.14 ± 0.24	28.65 ± 0.35	20.53 ± 0.25	8.10 ± 0.03	2.95 ± 0.03	0.92 ± 0.02
NGC 2841	10.48 ± 1.01	28.56 ± 0.98	47.83 ± 0.76	33.79 ± 0.22	15.93 ± 0.17	6.39 ± 0.09
NGC 2976	20.70 ± 1.17	37.32 ± 1.04	44.48 ± 1.88	25.30 ± 1.31	11.80 ± 0.73	4.81 ± 0.31
NGC 3077	20.67 ± 0.83	28.77 ± 0.77	27.72 ± 0.70	14.63 ± 0.92	6.93 ± 0.48	2.82 ± 0.18
NGC 3184	16.40 ± 2.11	36.60 ± 1.08	52.34 ± 1.00	33.03 ± 0.33	15.31 ± 0.25	6.22 ± 0.13
NGC 3198	10.54 ± 0.36	21.62 ± 0.64	29.12 ± 0.25	18.96 ± 0.07	9.91 ± 0.07	4.34 ± 0.06
NGC 3351	27.22 ± 1.42	48.04 ± 1.77	52.77 ± 0.76	33.00 ± 0.21	14.39 ± 0.19	5.28 ± 0.13
NGC 3521	80.62 ± 3.22	161.10 ± 1.75	199.98 ± 1.48	111.80 ± 1.02	47.87 ± 0.47	17.86 ± 0.20
NGC 3627	104.75 ± 1.41	183.48 ± 1.08	192.74 ± 0.93	94.25 ± 0.63	37.39 ± 0.27	12.95 ± 0.17
NGC 3938	16.82 ± 1.20	29.40 ± 1.04	38.72 ± 0.89	22.77 ± 0.19	10.24 ± 0.12	3.89 ± 0.09
NGC 4236	8.37 ± 1.65	13.83 ± 1.58	18.04 ± 1.03	11.06 ± 0.36	7.28 ± 0.26	3.97 ± 0.20
NGC 4254	57.34 ± 0.92	110.04 ± 0.94	124.98 ± 0.53	64.83 ± 0.33	26.05 ± 0.20	9.04 ± 0.13
NGC 4321	43.33 ± 1.23	86.57 ± 1.09	114.04 ± 0.66	65.87 ± 0.32	27.70 ± 0.26	9.70 ± 0.15
NGC 4536	40.22 ± 0.64	54.29 ± 0.46	53.77 ± 0.29	27.95 ± 0.09	12.49 ± 0.12	5.01 ± 0.09
NGC 4569	15.49 ± 0.52	31.32 ± 0.62	39.08 ± 0.44	22.05 ± 0.23	9.48 ± 0.15	3.43 ± 0.06
NGC 4579	10.10 ± 0.35	24.53 ± 0.52	33.39 ± 0.45	20.02 ± 0.09	8.66 ± 0.06	3.19 ± 0.03
NGC 4625	1.35 ± 0.20	3.34 ± 0.37	4.42 ± 0.24	2.66 ± 0.07	1.35 ± 0.06	0.58 ± 0.03
NGC 4631	141.22 ± 1.14	233.79 ± 1.17	238.95 ± 1.16	123.92 ± 0.23	56.22 ± 0.17	22.61 ± 0.12
NGC 4725	8.49 ± 1.00	25.47 ± 1.59	44.69 ± 0.56	31.64 ± 0.28	16.58 ± 0.20	7.10 ± 0.12
NGC 4736	103.66 ± 2.44	161.73 ± 4.27	137.47 ± 1.63	66.97 ± 0.66	27.69 ± 0.42	10.09 ± 0.22
NGC 5055	74.51 ± 3.61	174.72 ± 3.13	235.81 ± 2.00	145.67 ± 0.94	63.60 ± 0.46	24.05 ± 0.32
NGC 5457	127.51 ± 7.83	255.02 ± 5.17	320.70 ± 1.89	202.81 ± 0.92	98.17 ± 0.82	42.00 ± 0.44
NGC 5474	3.23 ± 0.82	4.88 ± 0.68	6.91 ± 0.43	5.14 ± 0.18	3.02 ± 0.09	1.48 ± 0.06
NGC 5713	28.83 ± 0.25	40.79 ± 0.17	37.19 ± 0.33	16.26 ± 0.08	6.25 ± 0.06	2.08 ± 0.03
NGC 6946	250.38 ± 5.60	447.29 ± 6.29	512.75 ± 4.63	268.77 ± 3.58	110.69 ± 2.16	39.46 ± 0.94
NGC 7331	68.11 ± 0.73	134.51 ± 1.01	167.65 ± 0.90	92.17 ± 0.59	39.94 ± 0.31	15.13 ± 0.15

Note. [a] Flux uncertainties include only uncertainties in background subtraction and noise.

in Dale et al. (2012) by sampling empty regions around our elliptical apertures and calculating the background mean and uncertainty, as well as the pixel noise. To determine the luminosities, we assume the distances given in Table 1. The total fluxes and uncertainties for all *Herschel* bands for each galaxy are given in Table 2. These fluxes differ slightly from those in Dale et al. (2012) as updated beam sizes were assumed for all bands leading to different correction factors, and the convolution to the SPIRE 500 μm beam size also affected results (though predominantly with the resolved investigations in Section 4).

In addition to the IR photometry, as the successor to the SINGS survey (Kennicutt et al. 2003), a large ancillary data set exists for the KINGFISH galaxies, including determinations of their metallicity, stellar masses, and SFRs, as shown in Table 1. The metallicities of our sample are determined in Moustakas et al. (2010), using the calibration of Kobulnicky & Kewley (2004), and cover a range of 2 dex. Different metallicity calibrations, such as Pilyugin & Thuan (2005, PT05), will introduce systematic offsets from the calibration used here (as demonstrated for several calibrations by Kewley & Ellison (2008), and as can be seen for the KINGFISH galaxies, specifically in Table 1 in Kennicutt et al. 2011).

2.3. Atomic Gas Masses

To determine the neutral gas mass of our galaxy sample, we use the THINGS H I sample of nearby galaxies (Walter et al. 2008),[11] with the addition of the Leroy et al. (2013a) sample that extends the THINGS sample to a larger number of nearby galaxies.

To determine the H I masses of the galaxies, we use the integrated H I moment 0 maps with robust weighting (see Walter et al. 2008 for details). To first convert the H I maps from their units of Jy beam^{-1} m s^{-1} to $M_{\odot}$ pc^{-2}, we multiply by (based on Equations (1) and (5) from Walter et al. 2008),

$$\Sigma_{\rm H\,I} = 8.667 \times 10^3 D^2_{\rm Mpc} S_{\rm H\,I}[{\rm Jy\,beam^{-1}}]/(B_{\rm maj} \times B_{\rm min}), \quad (1)$$

where $B_{\rm maj}$ and $B_{\rm min}$ are the beam major and minor axes in arcseconds, respectively. $D^2_{\rm Mpc}$ is the galaxy distance in megaparsecs (from Table 1). We then convolve the maps using first Gaussians to circularize the beam shapes and from there to the SPIRE 500 μm resolution using the convolution kernels

[11] The THINGS data are available from http://www.mpia-hd.mpg.de/THINGS.

Table 3
Integrated Gas Masses and 500 μm Luminosity of the 36 KINGFISH Galaxies

Galaxy	L_{500} $10^6\ L_\odot$	$M_{\rm H\,I}$ $10^7\ M_\odot$	$M_{\rm H2}$ $10^7\ M_\odot$
DDO053	0.12 ± 0.01	3.88 ± 0.58	<0.02
DDO154	0.19 ± 0.01	9.20 ± 1.38	<0.01
HoI	0.40 ± 0.02	10.06 ± 1.51	<0.03
HoII	0.89 ± 0.07	31.60 ± 4.74	<0.02
IC2574	4.93 ± 0.09	71.46 ± 10.72	0.82 ± 0.08
M81dwB	0.11 ± 0.01	0.92 ± 0.14	0.00
NGC 337	116.06 ± 0.63	330.82 ± 49.62	36.35 ± 1.82
NGC 628	121.05 ± 0.72	260.53 ± 39.08	127.41 ± 6.37
NGC 925	108.85 ± 0.37	448.59 ± 67.29	26.98 ± 1.35
NGC 2146	429.99 ± 1.24	188.07 ± 28.21	797.18 ± 39.86
NGC 2798	115.18 ± 0.93	72.72 ± 10.91	237.92 ± 11.90
NGC 2841	237.98 ± 0.81	450.51 ± 67.58	91.54 ± 4.58
NGC 2976	11.36 ± 0.10	12.72 ± 1.91	7.00 ± 0.35
NGC 3077	7.76 ± 0.05	28.94 ± 4.34	1.70 ± 0.09
NGC 3184	159.61 ± 0.92	302.38 ± 45.36	180.82 ± 9.04
NGC 3198	161.93 ± 0.44	506.31 ± 75.95	62.42 ± 3.12
NGC 3351	86.09 ± 0.54	95.24 ± 14.29	93.82 ± 4.69
NGC 3521	419.94 ± 0.87	811.43 ± 121.71	392.12 ± 19.61
NGC 3627	213.68 ± 0.61	87.40 ± 13.11	280.36 ± 14.02
NGC 3938	233.44 ± 1.84	432.18 ± 64.83	232.21 ± 11.61
NGC 4236	14.75 ± 0.14	203.74 ± 30.56	0.30 ± 0.02
NGC 4254	351.59 ± 0.90	381.34 ± 57.20	661.71 ± 33.09
NGC 4321	371.87 ± 0.98	257.89 ± 38.68	633.54 ± 31.68
NGC 4536	197.38 ± 0.72	363.38 ± 54.51	173.33 ± 8.67
NGC 4569	62.55 ± 0.31	19.86 ± 2.98	126.50 ± 6.33
NGC 4579	160.90 ± 0.60	57.18 ± 8.58	225.79 ± 11.29
NGC 4625	9.34 ± 0.16	32.12 ± 4.82	2.48 ± 0.12
NGC 4631	246.09 ± 0.31	616.84 ± 92.53	150.09 ± 7.50
NGC 4725	188.45 ± 0.79	294.52 ± 44.18	62.08 ± 3.10
NGC 4736	41.08 ± 0.24	40.70 ± 6.10	55.26 ± 2.76
NGC 5055	284.20 ± 0.94	365.07 ± 54.76	312.90 ± 15.65
NGC 5457	353.44 ± 0.74	888.70 ± 133.31	230.70 ± 11.54
NGC 5474	12.83 ± 0.16	69.06 ± 10.36	0.38 ± 0.02
NGC 5713	178.74 ± 0.79	197.49 ± 29.62	374.65 ± 18.73
NGC 6946	342.04 ± 1.38	409.18 ± 61.38	594.70 ± 29.73
NGC 7331	596.23 ± 1.21	901.71 ± 135.26	487.04 ± 24.35

of Aniano et al. (2012). The integrated H I masses are then determined using the same apertures as for the infrared fluxes and are given in Table 3 with uncertainties and SPIRE 500 μm luminosities. Note that for some galaxies the H I emission extends beyond the chosen aperture that encompasses the optical and IR emission, which we discuss further on.

2.4. Molecular Gas Masses

For the molecular gas masses of our galaxy sample, we use the HERACLES CO(2–1) survey of nearby galaxies (Leroy et al. 2009),[12] using the integrated moment 0 maps. To determine the total CO luminosity, we first convolve the moment 0 maps using the convolution kernels of Aniano et al. (2012), and then integrate using the same apertures as for the infrared and H I maps. If these apertures extended further than the available moment 0 maps, we assumed the flux in these regions was negligible and therefore 0. To convert the CO luminosity to molecular gas mass we used Equation (3) from Leroy et al. (2009),

$$M_{\rm H_2}[M_\odot] = \alpha_{\rm CO} R_{21} L_{\rm CO}[{\rm K\,km\,s^{-1}pc^2}]. \quad (2)$$

[12] The HERACLES data are available from http://www.mpia-hd.mpg.de/HERACLES/Overview.html.

We assume a fixed conversion factor from the CO(2–1) luminosity to H_2 mass for all galaxies, based on the Milky Way conversion factor, $\alpha_{\rm CO(1-0)} = 4.4\ M_\odot\ {\rm pc^{-2}}\ ({\rm K\,km\,s^{-1}})^{-1}$ (Solomon et al. 1987; Abdo et al. 2010; Bolatto et al. 2013), and a fixed line ratio of CO(2–1) to CO(1–0) of $R_{21} = 0.8$ (the typical value found for the HERACLES galaxies in Leroy et al. 2009, though correctly this ratio is dependent upon the mean gas properties such as temperature). The final H_2 mass for each galaxy is given in Table 3. The total gas mass for all galaxies is then taken simply as the sum of the H I and molecular gas mass within our chosen apertures.

Given that our galaxies cover over two orders of magnitude in stellar mass and gas-phase metallicity, an assumption of a constant CO luminosity to molecular gas mass conversion factor may lead to biases, especially as different conversion factors have already been determined for several of the galaxies in our sample (see, e.g., Bolatto et al. 2013; Sandstrom et al. 2013). We discuss this point further in the text, but this assumption must be considered when using any of our determined relationships.

3. THE MONOCHROMATIC IR–GAS CORRELATION

3.1. Dust Emission and Gas Mass

The use of the IR emission to trace the total amount of gas is premised on the simple assumption that gas and dust are always associated. Assuming that the dust has a single temperature, $T_{\rm d}$, the IR luminosity of a galaxy at a frequency, ν, is linked to the total gas mass of a galaxy $M_{\rm gas}$ via the equation,

$$L_\nu = M_{\rm gas}\left(\frac{D}{G}\right) 4\pi\, B_\nu(T_{\rm d})\kappa_\nu, \quad (3)$$

where (D/G) is the DGR, B_ν is the Planck blackbody function, and κ_ν is the dust emissivity at the frequency ν.

A broad range of IR colors is seen within and between galaxies indicating variation of the mean dust temperature (see, e.g., Dale et al. 2012), driven by the variation of radiation field strengths experienced by dust in galaxies. However, we can limit the impact of these temperature distributions on the above equation in two ways. First, for most of the KINGFISH galaxies, it is possible to reproduce their IR SED by having the bulk of the dust heated by a single diffuse radiation field, with only a small fraction being heated by radiation fields stronger than this (see, e.g., Draine et al. 2007; Aniano et al. 2012); thus, assuming a single temperature within galaxies for the longer wavelengths is a reasonable assumption. Second, by concentrating on longer wavelengths that are well past the peak of the IR SED (at ~100–200 μm, see, e.g., Dale et al. 2012), we move closer to the Rayleigh–Jeans tail of the black body radiation, which is only linearly sensitive to temperature. Smith et al. (2012, particularly their Figure 7) and Auld et al. (2013, particularly their Figure 12) have both shown that the assumption of a single temperature is reasonable, finding the temperatures of single modified blackbody fits to the integrated 100–500 μm IR SEDs of galaxies in the *Herschel* Reference Survey and *Herschel* Virgo Cluster Survey, respectively, lying within a factor of two (25 ± 10 K and $\sim 20 \pm 8$ K, respectively, with early-type galaxies having higher temperatures). Such a small range of temperatures result in only a factor of approximately two uncertainty in the dust mass estimates and hence a factor of two in the gas mass determined from the IR in the linear regime.

The dust to gas mass ratio and dust emissivity at a given wavelength are somewhat degenerate, with the determination

Table 4
Correlation Coefficients for log(M_{gas}) Against Individual *Herschel* Bands

Band (log(νL_ν))	Pearson	Spearman
PACS70[a]	0.926	0.821
PACS100	0.938	0.893
PACS160	0.943	0.918
SPIRE 250	0.949	0.941
SPIRE 350	0.957	0.950
SPIRE 500	0.962	0.964

Note. [a] Correlation does not include DDO154, which is not detected at 70 μm.

of one relying on an estimate of the other. While estimates exist for these quantities in the local group, it is uncertain how they will vary across different galaxies. The emissivity is dependent on the composition of dust (Zubko et al. 2004), and there have been suggestions that the emissivity will vary in molecular environments. The emissivity has also been suggested to vary with metallicity, such as seen in the LMC by Galliano et al. (2011), however, Rémy-Ruyer et al. (2013) found no strong trends when comparing more massive galaxies with dwarf galaxies. However, if it is assumed that emissivity at longer wavelengths does not change between galaxies, a clear trend of a decreasing DGR with the metallicity of the galaxy is seen across the local group (Leroy et al. 2011) and nearby galaxies (Sandstrom et al. 2013), and even if the emissivity is left free, a lower DGR is seen in low metallicity dwarf galaxies (Rémy-Ruyer et al. 2014). This suggests that the DGR must be accounted for in any empirical calibration, as we discuss below.

Although Equation (3) indicates the direct link of gas mass and dust emission via the association of dust and gas, IR emission will also be indirectly associated with gas mass, or more precisely gas-mass surface density via the K-S relation (see, e.g., Kennicutt 1998). An increase in the gas-mass surface density has been empirically demonstrated to correlate on average with an increase in the SFR surface density on kiloparsec scales (see, e.g., Kennicutt 1998; Bigiel et al. 2008; Leroy et al. 2013b). Given this increase in the SFR surface density, the interstellar radiation field that heats the dust is also expected to be higher, leading in turn to higher average dust temperatures and correspondingly higher IR continuum emission. This secondary correlation may actually limit the dispersive effect that dust temperature has on the gas mass–IR emission connection, and may even lead to a tighter correlation where the IR luminosity is more responsive to gas mass (i.e., where an increase in gas mass leads to both an increase in dust mass and increase in dust temperature due to the increased SFR, and thus a greater increase in IR luminosity). However, unlike the correlation of dust mass and gas mass, the K-S relation will act nonlinearly on the IR emission. The shortest dust wavelengths that measure the hot dust and peak of the IR emission will see the greatest impact of the increase in dust temperature, and thus also be more sensitive to any variation in the K-S relation.

3.2. IR Emission versus Total Gas Mass

As a first comparison, we determine the simple correlations between the IR luminosities and total gas mass in galaxies. In Table 4, we show the Pearson correlation coefficient (& Spearman rank coefficient) for all *Herschel* bands against the total gas mass. A strong correlation is observed with all bands, with the strongest correlation existing between the longest wavelength (i.e., SPIRE 500 μm) and the total gas mass. This correlation is clearly seen in Figure 1, where we plot the SPIRE 500 luminosity (νL_ν) against the total gas mass.

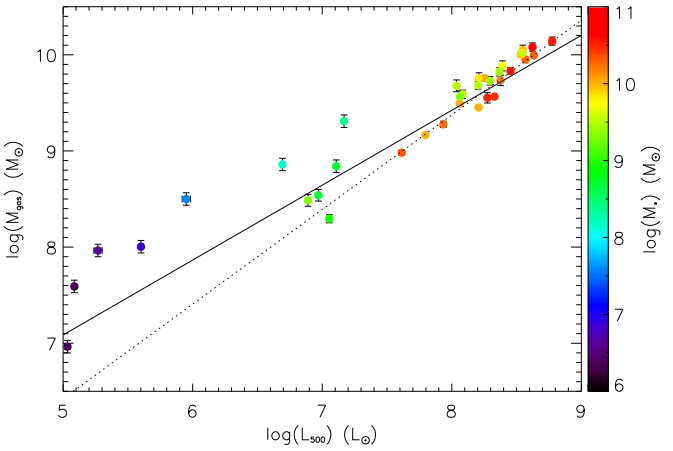

Figure 1. SPIRE 500 luminosity (L_{500}) vs. total gas mass M_{gas} for the KINGFISH sample. The colors correspond the total stellar mass of the galaxy, as indicated by the color bar to the right. Over plotted is the linear fit to the full sample (solid line), and only to the non-dwarf galaxies ($\log(M_\star/M_\odot) > 9$, dashed line), with the fit values given in Table 5.

Table 5
Coefficients of Linear Fits of the Form $\log(M_{gas}) = A + B \times$Band

Band (log(νL_ν))	All			$\log(M_\star/M_\odot) > 9$		
	A	B	σ	A	B	σ
PACS70[a]	4.15	0.55	0.30	4.6	0.50	0.27
PACS100	3.62	0.60	0.27	3.27	0.63	0.23
PACS160	3.52	0.61	0.26	1.91	0.78	0.18
SPIRE 250	3.17	0.69	0.25	1.17	0.90	0.15
SPIRE 350	3.08	0.74	0.24	1.17	0.90	0.14
SPIRE 500	3.19	0.78	0.23	1.44	0.99	0.10

Note. [a] Correlation does not include DDO154, which is not detected at 70 μm.

The strong correlations seen with each band suggest that it is entirely reasonable to use broadband IR photometry to estimate the total gas mass of galaxies from the IR emission. Based on the high Pearson correlation coefficients, we performed robust linear fits to each *Herschel* band luminosity versus the total gas mass, of the form, $\log(M_{gas}) = A + B \times$ Band, where Band is the log of the luminosity in the given band (in log(νL_ν)). The coefficients A and B are given in Table 5 for each band. The fit for the SPIRE 500–M_{gas} relation is shown by the solid line on Figure 1. In Table 5, we also give the dispersion, σ, of the galaxies around each relation, which, as suggested by the correlation coefficients, decreases with increasing wavelength. To compare with previous comparisons of dust and gas correlations, we have also limited the sample to the more massive objects, with $\log(M_\star/M_\odot) > 9$. The fits to these galaxies show both a smaller dispersion and steeper slopes than the full sample. The SPIRE 500 fit is the tightest, with only a 30% dispersion, similar to that found by Eales et al. (2012) in their comparison of gas masses with dust masses determined from fits to the IR SED in 10 nearby galaxies.

Given that the full extent of a galaxy in the IR may not always be available, we have also repeated the fits using smaller apertures that are truncated at an optical radius, R_{25}, using the values for the major and minor axes presented in Table 1. These apertures are typically 30% smaller than the IR-encompassing apertures from Dale et al. (2012) that we use. However, as the IR

Table 6
Linear Fit Coefficients for Galaxies Measured within R_{25}

Band ($\log(\nu L_\nu)$)	All			$\log(M_\star/M_\odot) > 9$		
	A	B	σ	A	B	σ
SPIRE 250	3.73	0.64	0.28	1.57	0.86	0.14
SPIRE 350	3.63	0.68	0.25	1.49	0.92	0.10
SPIRE 500	3.74	0.72	0.23	1.72	0.96	0.09

light is generally concentrated to the optical disk, these smaller apertures contain a significant fraction (>90%) of the IR light for most galaxies. Only a few galaxies with clearly extended IR emission, mostly the smaller galaxies such as NGC 3077, have significantly reduced IR fluxes due to the smaller aperture. Similarly, most of the molecular gas is totally contained within an optical radius for all galaxies. However, the atomic gas can extend well beyond an optical radius, and is observed at greater than $3R_{25}$ in some galaxies. Truncating at R_{25} reduces the total gas mass because of this extended emission (this is discussed further in Section 4). We have performed these fits only for the three SPIRE bands, as these show the strongest correlations in Table 4, and are the most sensitive to extended emission (and thus show the greatest change with reduced apertures). All fits to the reduced apertures (listed in Table 6), both to the full and non-dwarf galaxy subsample, find slightly flatter slopes than the original apertures, leading also to a larger intercept. This trend is driven by the dwarf galaxies, which have relatively larger H I gas disks, such that the smaller aperture preferentially reduces the gas mass relative to the IR, flattening the overall slope. Thus biasing an aperture to measure the IR luminosity of galaxy will tend to underestimate the total gas mass, approximately by 15% based on our galaxy sample.

We find that none of the fits are linear, neither the total gas masses and the sample limited within R_{25}, nor the massive galaxy subsamples in both, with all slopes less than one. As discussed in the previous section, three factors may be playing a role in the nonlinear slopes: the systematic variation of the dust temperature, the DGR, and the variation of the CO luminosity to molecular gas mass (α_{CO}). As the slope becomes flatter at shorter wavelengths, dust temperature must play at least some role. The sublinear trend observed in the correlation at all wavelengths suggests that the K-Srelation may also be contributing to the correlation, that is higher gas masses lead to a higher SFRs, which in turn heats the dust to higher average temperatures.

The dependence upon the CO conversion factor is a major source of uncertainty in these fits and remains a general uncertainty in determining the total gas masses in galaxies. Our assumed value of $\alpha_{CO(1-0)} = 4.4\ M_\odot\,pc^{-2}\,(K\,km\,s^{-1})^{-1}$ is the suggested value of the Milky Way conversion factor given in the extensive review of Bolatto et al. (2013). However, the analysis of α_{CO} in some of the same galaxies as our sample by Sandstrom et al. (2013) found a slightly lower value ($\alpha_{CO} = 3.6$), and a large scatter between, and within, the galaxies. Changing the value of α_{CO} we assume significantly affects only the more massive spirals ($M_\star > 10^9\,M_\odot$), as the dwarf galaxies are all H I dominated, as can be seen from Table 3. Increasing/decreasing α_{CO} by 0.7 dex (larger than the dispersion between galaxies found by Sandstrom et al. 2013) leads to a steepening/flattening of the determined linear fits. However, when only the galaxies with $M_\star > 10^9\,M_\odot$ are examined, the slope remains approximately constant, with a systematic shift up and down in the relation, scaling with our scaling of α_{CO}. However, given the work of Sandstrom et al. (2013) and review by Bolatto et al. (2013), there is no a priori reason why our normal spiral galaxy sample should have a different α_{CO} to that assumed in our work.

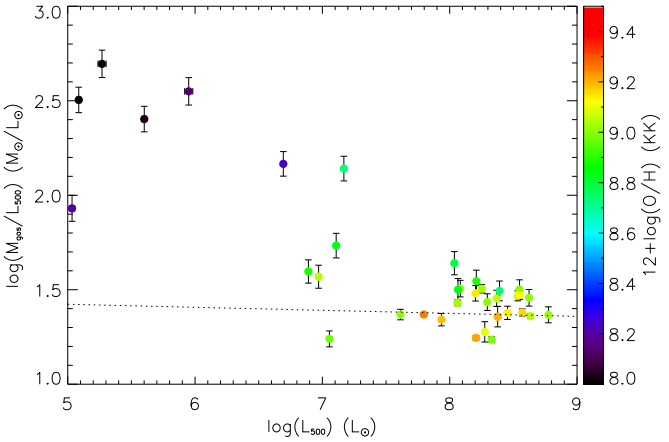

Figure 2. SPIRE 500 μm luminosity (L_{500}) against the ratio of the total gas mass M_{gas} to L_{500}. The colors in this figure show the average metallicity of the galaxies, as measured by Moustakas et al. (2010), using the Kobulnicky & Kewley (2004) conversion. This figure clearly indicates the linear relationship between M_{gas} and L_{500} for non-dwarf galaxies, and the offset of the low stellar mass (low metallicity) galaxies.

However, there are two further issues with the simple linear fits revealed by Figure 1; a large part of the correlation of gas mass with IR luminosity is simply galaxy mass scaling, with galaxies with the highest stellar masses lying toward the top right, as indicated by the color of the points. Secondly, the lower mass galaxies tend to lie above the relation, leading to a much greater scatter, and limit the determination of the gas mass. In Figure 2, we remove the mass weighting intrinsic to a luminosity–luminosity plot by plotting the ratio M_{gas}/L_{500} against L_{500}, which also emphasizes the scatter of the low-mass galaxies. The color scale in this figure reveals the average metallicity of the galaxy, as measured by Moustakas et al. (2010; using the Kobulnicky & Kewley 2004 conversion). The similarity in colors between the two plots demonstrates the mass–metallicity relation. In this figure, it is clear that the more massive normal galaxies show a much more linear relation, with the offset caused by the low-mass, low-metallicity galaxies in the sample. In Table 6, we also include a fit to only the galaxies with $\log(M_\star/M_\odot) > 9$) (non-dwarf galaxies, hereafter "normal" galaxies), meaning a $12 + \log(O/H)_{KK} \gtrsim 8.6$ using the Kewley & Ellison (2008) mass–metallicity relation). This is shown as the dashed line in Figures 1 and 2 which emphasizes the difference to the full-sample fit. As clear from these figures and Table 6, the dispersion of the normal galaxies around the normal galaxy-only fit is reduced relative to that of that seen around the full-galaxy relation. The largest decrease in dispersion appears to be for the longest wavelengths, with the SPIRE 500 relation decreasing by a factor of two, while the dispersion at the shortest wavelengths only decreases slightly.

As the relation for the SPIRE 500 and M_{gas} is almost linear for normal galaxies, we can naively assume a one to one relation. In this case, we find for the normal KINGFISH galaxies ($M_* > 10^9\ M_\odot$);

$$M_{gas}[M_\odot] = 28.5\,L_{500}[L_\odot], \quad (4)$$

where L_{500} is the SPIRE 500 μm luminosity (i.e., νL_ν). Assuming a linear correlation at 500 μm only increases the dispersion slightly to 0.118 dex (i.e., most gas masses within 30%).

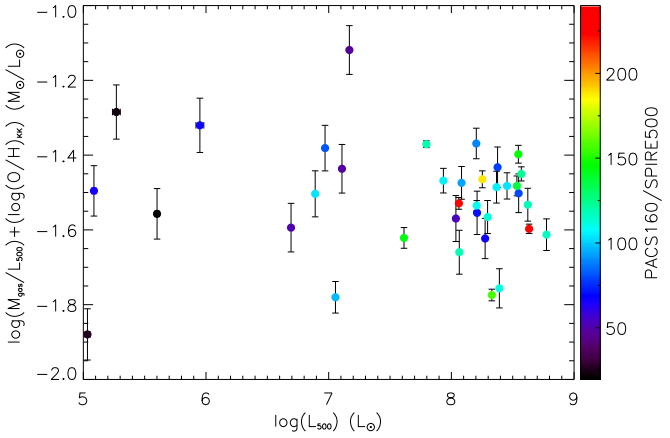

Figure 3. SPIRE 500 luminosity (L_{500}) against the ratio of the total gas mass $M_{\rm gas}$ to SPIRE 500 luminosity as in Figure 2, however corrected for the variation of the dust to gas ratio by multiplying each galaxy by the average metallicity determined by Moustakas et al. (2010). This assumes a linear scaling between the metallicity and dust to gas ratio. Note that the shown uncertainties do not include that on the metallicity, which can be large and systematic. The color scale shows the 160 μm/500 μm flux ratio, a proxy for dust temperature where a lower value indicates warmer dust, and demonstrates that temperature effects do not dominate the observed spread in the corrected ratio.

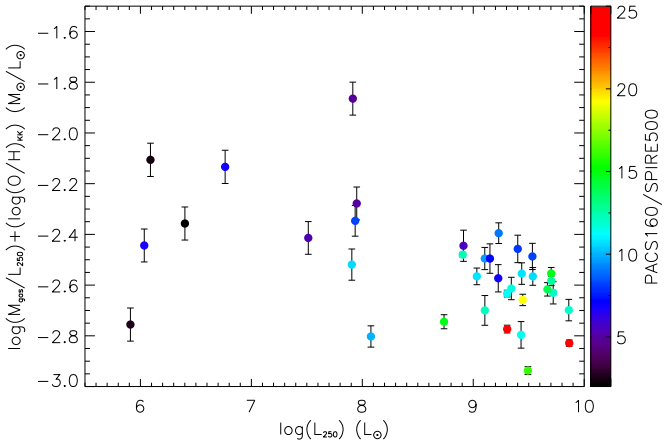

Figure 4. Same as Figure 3, but substituting the SPIRE 250 luminosity (L_{250}) for L_{500}. The colors show the PACS160/SPIRE 500 color, a measure of the mean dust temperature, where a lower value indicates warmer dust.

One issue with the linear relations we present is that they are only monochromatic, and that these rest-frame wavelengths may not be available at higher redshifts when observed using for example *Herschel* or ALMA. In these cases, we suggest a simple linear interpolation of the slope, B, and constant, A in Table 6. The slope is monotonic, at least within the range of wavelengths explored here, and thus a simple linear interpolation should suffice. For the constant, there appears to be a minimum at 350 μm; however, again a linear interpolation between the bounding wavelengths should be sufficient and lead to only a small uncertainty (as seen by the range of A), except at the shortest wavelengths. For continuum measurements outside the range explored by *Herschel*, an extrapolation based upon a simple modified blackbody can be applied (as done for Equation (10) in Scoville et al. 2014).

3.2.1. The Effects of Metallicity

The offset observed at low stellar masses in Figure 2 is clearly associated with a decline in the gas phase metallicity. Given this, the most likely cause for this offset is the variation of the DGR with metallicity. Naively, we would expect the DGR to at least linearly decrease with metallicity due to the lack of metals from which to form, with recent works suggesting that a linear DGR to metallicity relation is a reasonable assumption (Leroy et al. 2011; Sandstrom et al. 2013; Rémy-Ruyer et al. 2014, though the latter work suggests this is true only for $12+\log({\rm O/H}) \gtrsim 8$). In Figure 3, we have used the measured metallicity of our galaxies from Moustakas et al. (2010) to "correct" for a linear variation of the DGR by scaling the $M_{\rm gas}/L_{500}$ ratio by O/H. With this correction included, the relationship between $M_{\rm gas}/L_{500}$ and L_{500} is basically flat (a fitted slope of -0.008), and a dispersion of only $\sigma_{500} = 0.147$, much less than the original fits to all galaxies. Thus, over four orders of magnitude in IR luminosity, the total gas mass can be determined from the 500 μm luminosity within $\sim$40%, as long as the effects of metallicity on the DGR can be corrected for.

One issue in correcting for the variable DGR is the difficulty in obtaining the gas-phase metallicity of a galaxy at higher redshift. When such information is not available, using the mass–metallicity relation, presuming a stellar mass for the galaxy has been determined, provides one possible solution (see, e.g., Tremonti et al. 2004; Kewley & Ellison 2008).

The metallicity of the ISM also affects the relation of dust and gas through the CO luminosity to the molecular gas-mass conversion factor $\alpha_{\rm CO}$. For the lowest metallicity galaxies, $\alpha_{\rm CO}$ may increase by an order of magnitude or more from the Milky Way value assumed here because of the presence of "CO–dark" molecular gas (see, e.g., Wolfire et al. 2010; Leroy et al. 2011, for the theory and for examples and discussion in the local universe). However, as mentioned in the previous section, the "low-mass galaxies" in our sample all have molecular gas fractions less than 0.01 (given our assumed Milky Way conversion factor, as seen in Figure 5 in the following section), meaning that the contribution of molecular to the total gas mass in these objects will always be relatively small. This effect will act to increase the offset we observe in Figure 2, but will contribute less than a factor of two (0.3 dex) to any relation.

While the correction for metallicity clearly works for the $M_{\rm gas}$–L_{500} relation at long wavelengths, at shorter wavelengths the effect of dust temperature is still an issue, as suggested by the flattening of the slopes in Table 6. Figure 4 shows the relation of the SPIRE 250 luminosity with $M_{\rm gas}$ corrected for the variable DGR, as in Figure 3, with both the negative slope and increased scatter compared to the L_{500} relation are noticeable. The color of the points indicates the PACS160/SPIRE 500 color, which we use as a proxy for the dust temperature, where a lower value indicates warmer average dust temperatures as the peak of the IR shifts to wavelengths shorter than 160 μm. Note how at high masses (high L_{250}), a higher $M_{\rm gas}/L_{250}$ is seen with a decreasing 160/250 ratio, indicative of warmer temperatures. However, with the $M_{\rm gas}/L_{500}$ plot (Figure 3) no such gradient is seen with the PACS160/SPIRE 500 ratio, demonstrating the lack of sensitivity of the longer wavelength emission to dust temperature. This suggests, not unexpectedly, that to obtain a more accurate gas mass at shorter wavelengths, at least two bands must be observed to correct for dust temperature. However, given that the IR continuum at or around 500 μm (600 Ghz) is observable at essentially all redshifts up to $z \sim 6$ using existing ALMA bands (and longer using bands 1 and 2), and no sensitivity to the IR colors is seen in the scatter at these

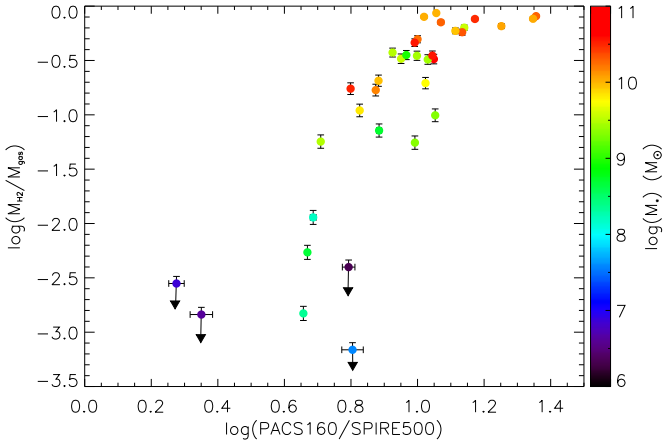

Figure 5. Molecular gas fraction (M_{H2}/M_{gas}) as a function of the PACS160/SPIRE 500 flux ratio, a proxy for mean dust temperature (low values indicate warmer dust). The color scale indicates the total stellar mass of the galaxies.

wavelengths, we suggest using longer rest-frame wavelengths when possible to determine the total gas mass.

3.3. IR Emission versus Molecular Gas Mass

Given that the SFR surface density in nearby galaxies appears to correlate better with the molecular gas surface density than the total gas density (e.g., Schruba et al. 2011), determining the molecular gas mass at higher redshift without the necessity of measuring a possibly weak line would be useful. When we compare the molecular gas mass (or, more precisely, CO(2–1) luminosity) to the infrared luminosities for our full sample of galaxies we find the wavelengths at the peak of the IR SED (100 and 160 μm) show the tightest correlation, with Table 7 listing the Pearson correlation coefficient and Spearman rank coefficient for each *Herschel* band for the correlation. We find that this is true even when we limit the sample to the normal galaxies. This is somewhat contrary to Bourne et al. (2013), who found the highest correlation of the molecular gas mass with the longest wavelengths.

This is surprising given that molecular gas would be expected to be cold, and therefore mostly associated with cold dust. However, a closer examination reveals that this is exactly the case, as demonstrated in Figure 5. In this figure, we plot the molecular gas-mass fraction, M_{H2}/M_{gas}, as a function of the dust temperature as represented by the PACS160/SPIRE 500 flux ratio (a higher ratio indicates colder dust as the IR peak shifts to 160 μm). Given that the denominators correlate, as shown in Figure 1, this removes any mass scaling, and acts to highlight the correlation between the 160 μm luminosity and molecular gas mass indicated in Table 7. This figure reveals that as the dust gets colder (higher 160 μm/500 μm) the molecular gas fraction increases, with both these quantities correlated with the galaxy stellar mass (as shown by the color scale in Figure 5), or similarly the average gas metallicity.

The evolving shape of the IR SED with the metallicity of the galaxy can be seen clearly in Figure 8 in Rémy-Ruyer et al. (2013), demonstrating the warmer average dust temperatures in the lower metallicity objects. The warmer temperatures in these galaxies are likely caused by the harder and stronger interstellar radiation fields (ISRF). The ISRF is harder due to the lower stellar metallicity in these galaxies, while the ISRF tends to be stronger due to the lower dust density (given the lower DGR) leading to decreased dust shielding and a longer mean free path of UV photons (Madden et al. 2006).

This lower dust shielding will lead to a lower molecular gas fraction due to increased H_2 dissociation, and a relatively higher dissociation of the CO molecule, and thus an increased α_{CO} factor. As we assume a constant α_{CO} factor, an increasing α_{CO} with metallicity (due to the presence of "CO–dark" molecular gas, Wolfire et al. 2010), will also cause the decrease in the molecular gas fraction that we observe (if a variable α_{CO} is assumed, it is uncertain how much the molecular gas fraction will change with metallicity, see, e.g., Rémy-Ruyer et al. 2014, specifically their Figure 3).

Once the correlation of these ratios with stellar mass is accounted for, no association with other galaxy parameters such as SFR or sSFR is seen (note, however, that these parameters correlate with stellar mass in our galaxy sample, as seen in SDSS galaxies, e.g., Brinchmann et al. 2004). This is surprising, given that the 160/500 ratio traces dust temperature, and that molecular gas is associated with star formation. However, it may be that smaller scale effects not seen in the integrated quantities, such as the spatial distribution of gas, dust, and stars, is affecting the correlation to an extent that second order effects are not seen.

In general, we find the best power-law fit to be

$$\log M_{H2}[M_\odot] = -2.86 + 1.22 \log(\nu L_\nu(160\,\mu\mathrm{m})/L_\odot) \quad (5)$$

with a dispersion of $\sigma = 0.32$ around this relation. However, once a galaxy is molecular rich, it is uncertain how well the 160 μm luminosity will trace M_{H2}. As can be seen in Figure 5, at high molecular fractions, a broad range of 160 μm/500 μm colors are possible. Thus for the most massive objects, the 500 μm luminosity is a better tracer of the molecular gas simply because $M_{H2}/M_{gas} \sim 1$. Similarly, given the uncertain effects of dust heating on this relation, extrapolating this to higher redshifts may be problematic.

3.4. Extension to Higher Luminosities and Redshifts

The sample of galaxies we explore here are typical local galaxies, and cover a range of luminosities and stellar masses (as seen in Table 1); however, these galaxies may not be representative of more luminous IR galaxies typically seen in submillimeter surveys. Bourne et al. (2013) explore a slightly higher mass range than our sample, though with a significant overlap. For our full sample, we find much flatter slopes than Bourne et al. (2013) found for the IR versus H I, CO(2–1) and CO(3–2) luminosities. However, for our more massive "normal" galaxy sample that overlaps the range observed in Bourne et al.

Table 7
Correlation Coefficients for $\log(M_{H2})$[a]
Against Individual *Herschel* Band Luminosities

Band ($\log(\nu L_\nu)$)	All		Mass Selected	
	Pearson	Spearman	Pearson	Spearman
PACS70[b]	0.957	0.929	0.905	0.890
PACS100	0.979	0.955	0.946	0.925
PACS160	0.977	0.969	0.959	0.949
SPIRE 250	0.980	0.958	0.951	0.932
SPIRE 350	0.974	0.936	0.933	0.895
SPIRE 500	0.964	0.901	0.908	0.836

Notes.
[a] M81 dwarf B is not detected in CO, and is not included.
[b] Correlation does not include DDO154, which is not detected at 70 μm.

(2013), our slopes appear very similar to those determined by Bourne et al. (2013, specifically their Figure 4), at least for H I and CO(2–1), the lines we use for our total gas mass. However, while they do see trends with stellar mass and metallicity (such as the decrease in $L_{CO}/M_{H\,I}$ with mass and metallicity), their dynamic range is not large enough to determine the relations we see here.

Scoville et al. (2014) explored the correlation of submillimeter luminosity with ISM mass in a sample of submillimeter galaxies at $z = 2$–3, in addition to a local sample that overlaps our sample with 850 μm detections, and a Planck observation of our Galaxy. Assuming that all the gas was molecular and a similar conversion factor ($\alpha_{CO} = 4.6$), Scoville et al. (2014) find a ratio of $L_{850}/M_{gas} = \alpha_{850} = 1 \pm 0.5 \times 10^{20}$ erg s^{-1} Hz^{-1} $M_{\odot}^{-1}$ for the submillimeter galaxies, and similar values for the local galaxies (for which the H I mass was also included). Rearranging Equation (4), we find a ratio at 500 μm of $\alpha_{500} = 2.26 \times 10^{20}$ erg s^{-1} Hz^{-1} $M_{\odot}^{-1}$ for our normal galaxy sample, which, assuming a dust emissivity with a power law of 1.8, corresponds to $\alpha_{850} = 0.3 \times 10^{20}$ erg s^{-1} Hz^{-1} $M_{\odot}^{-1}$, in good agreement with the submillimeter galaxy sample of Scoville et al. (2014).

However, applying a single submillimeter emission to gas-mass conversion factor, α, to all galaxies removes any dependence on other galaxy properties. We find that for normal galaxies in the local universe, an assumption of a linear relation between submillimeter luminosity and gas mass is reasonable. Given the range of IR luminosities explored in our work and in Scoville et al. (2014), it suggests that, while dust temperatures will affect the submillimeter luminosity to gas-mass relationship, the variation in temperature is small enough that it has only a small impact in the Rayleigh–Jeans regime and thus the relationship. Conversely, there appears to be a significant metallicity evolution over cosmic time (see, e.g., Yabe et al. 2014). Therefore, to apply the observed $L_{submillimeter}$–M_{gas} relation to all galaxies at higher redshifts, it is crucial that this evolution of the metallicity be accounted for. This can be done through a direct correction for an inferred metallicity, either directly measured or determined from a mass–metallicity relation, or through allowing the relation (or α) to evolve with redshift using the metallicity evolution as a basis for the evolving DGR.

An evolving DGR was allowed for in the work of Magdis et al. (2011, 2012), who calculated the total gas mass from IR observations in a sample of "normal" high-redshift galaxies ($z \sim 1$–4). Instead of using a direct correlation of submillimeter luminosity and gas mass, they first calculated the dust mass using model fits to their observed IR SEDs (such as the Draine & Li 2007, model), and then converted to the total gas content using an empirical relationship between the DGR and metallicity determined locally (Leroy et al. 2011). While this two-step approach may introduce systematic errors, Magdis et al. (2012) find their determined gas masses consistent with the CO luminosities (assuming Milky Way conversion factors that also vary with metallicity, and assuming the gas is mostly molecular).

An example of the application of using IR fluxes to determine the evolution of gas mass is the work of Santini et al. (2014), who stacked the IR fluxes of galaxies with similar stellar masses, SFRs and redshifts, to create representative IR SEDs. They then fit these SEDs using dust models, including simple modified blackbodies, to determine the dust masses of these objects, which they converted to a gas mass allowing for a variable DGR dependent upon stellar mass and SFR. Using these they find a strong correlation in the gas fractions of galaxies with their stellar mass and SFRs, and find strong evolution in both the gas fraction and star formation efficiency (SFR/M_{gas}) with redshift.

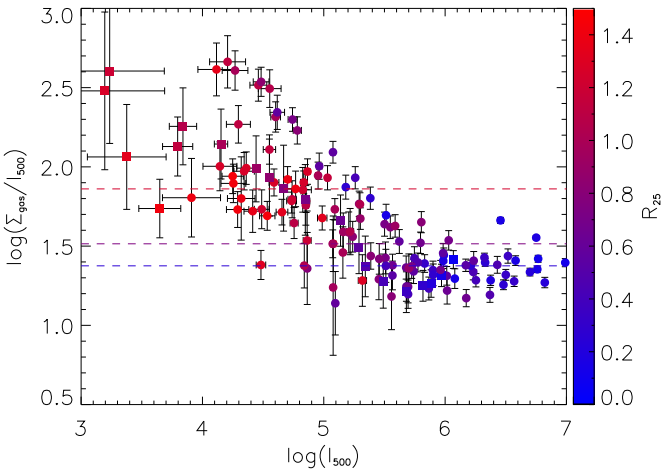

Figure 6. SPIRE 500 μm luminosity (L_{500}) against the ratio of the total gas mass M_{gas} to L_{500} (following Figure 2), measured in elliptical annuli of $\Delta r = 2$ kpc for galaxies in our sample. The colors indicate the position of the annuli in terms of the optical radius R_{25} of each galaxy, as given in Table 1. The dashed horizontal lines indicate the median S_{gas}/I_{500} ratio for annuli between 0–0.5, 0.5–1.0, and 1.0–1.5 R_{25} as indicated by the colors.

4. RADIAL TRENDS AND GALAXY SIZES

In the previous section, we only considered the galaxies as integrated objects, with a single gas mass and luminosity. However, the KINGFISH sample provides much more detail than this, and the subarcsecond capabilities of ALMA will mean, even at high redshift, the continuum emission from galaxies can potentially be resolved (see, e.g., Hodge et al. 2013). Thus to explore the gas–L_{500} relation further, we break the galaxies into elliptical annuli using the position angles and axis ratios of the galaxies given in Table 1. The annuli are chosen to be in steps of 2 kpc along the major axis

In Figure 6, we plot the ratio of the gas-mass surface density and SPIRE 500 surface brightness for all annuli in our galaxy sample that satisfy the criteria that the annuli was larger than the resolution of the SPIRE 500 μm beam (36″). The colors of the data indicate the position of the annuli in terms of the optical radius R_{25} of each galaxy, as given in Table 1. This figure demonstrates that within galaxies the radial profiles follow the same pattern as seen for the integrated luminosities (i.e., as in Figure 2), albeit with a larger scatter. Some of this scatter arises from faint background sources at large radii that have not been masked. As with the luminous galaxies, we see that for high surface brightness regions Σ_{gas}/I_{500} is linear, but when we move to lower I_{500} we find an increasing trend of Σ_{gas}/I_{500}. This trend is affected by both the intrinsic metallicities of the galaxies as well as the radial trends within galaxies, with a higher Σ_{gas}/I_{500} ratio observed at larger radii. This is emphasized by the horizontal lines, which indicate the median Σ_{gas}/I_{500} ratio for annuli between 0–0.5 (blue), 0.5–1.0 (purple), and 1.0–1.5 R_{25} (red). This radial Σ_{gas}/I_{500} gradient is likely associated with the radial metallicity gradient within each galaxy, and when the observations are corrected for the metallicity gradient determined by Moustakas et al. (2010) for some of our sample, this gradient is reduced. However, the gradient is not totally removed, and has a large scatter introduced

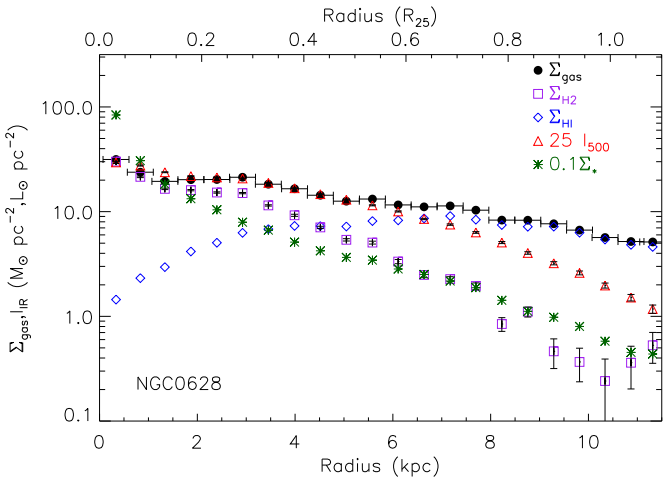

Figure 7. Radial variation of the SPIRE 500 surface brightness, $I_{\rm IR}$ (triangles), and the H I (diamonds), H_2 (squares), and total gas (solid circles) and stellar mass (stars) surface densities in bins of 15″ in NGC 628. The SPIRE 500 surface brightness and stellar-mass surface density have been scaled by 25 and 0.1, respectively, to place these on the same scale as the gas mass surface densities. The H I, H_2, and total gas mass surface densities are from Schruba et al. (2011), and the stellar mass surface density is from Querejeta et al. (2014).

(The complete figure set (28 images) is available.)

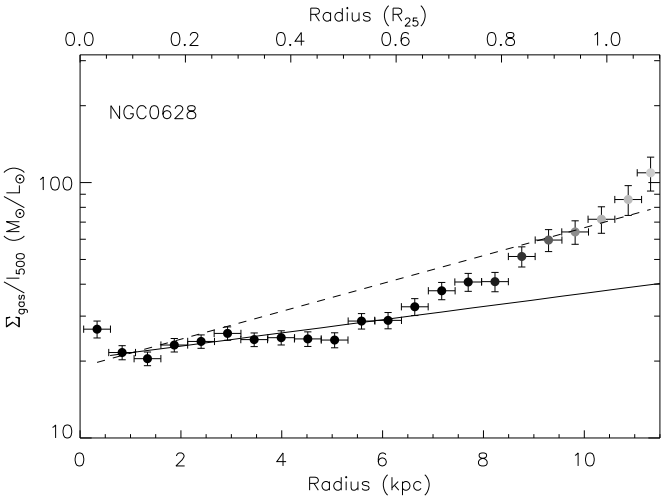

Figure 8. Radial variation of the ratio of gas–mass surface density to SPIRE 500 surface brightness, $\Sigma_{\rm gas}/I_{500}$ for the face on spiral NGC 628. At $\sim 0.7 R_{25}$, a change in how the ratio varies with radius is visible. The grayscale shading of the data indicate the fraction of significant pixels with signal to noise greater than three. Overplotted are two lines showing the inverse of the metallicity gradient determined by Moustakas et al. (2010) using the Pilyugin & Thuan (2005) (solid line) and Kobulnicky & Kewley (2004) (dashed line) calibrations. Both lines have been normalized to the value of $\Sigma_{\rm gas}/I_{500}$ at $0.1 R_{25}$.

(The complete figure set (28 images) is available.)

by the uncertainties in the metallicity gradient (see Moustakas et al. 2010, for a discussion on these uncertainties).

Though, using the longer wavelength continuum emission is still a robust tracer of the total gas mass of galaxies, and the gas surface density for most of a galaxy. The robustness of the submillimeter continuum can be seen in Figure 7, where we compare the radial variation of the SPIRE 500 mean surface brightness, I_{500}, against the mean gas-mass surface density, $\Sigma_{\rm gas}$, in NGC 628. Using the radial determinations of the H I and H_2 gas mass surface densities from Schruba et al. (2011), who stacked the HERACLES CO observations to detect the low column density molecular gas at large radii, we can determine both the radial variation of the total gas mass and the molecular gas fraction in our sample. Using the same 15″ elliptical annuli as Schruba et al. (2011), we have determined the radial variation of the SPIRE 500 surface brightness (note that 15″ under samples the 36″ SPIRE 500 beam by a factor of three). For illustration purposes, we have scaled I_{500} by a factor of 25 to be on the same scale as the total gas-mass surface density. It is clear that the IR traces better the total gas-mass surface density instead of either the H_2 or H I gas alone in the inner radii. However, at radii beyond 0.7 R_{25} there is an increasing deviation of the IR brightness relative to the gas mass density. A similar trend is seen for some of the other galaxies in our matched sample, such as NGC 925. However, the trend is not seen in all galaxies, with resolution and inclination affecting the observed trends in some objects (see the Figure sets associated with Figures 7 and 8).

The point where the submillimeter surface brightness and gas-mass density separate does not appear to directly correlate with the radius at which the gas becomes mostly atomic, emphasizing that the dust is not just tracing the molecular gas. This conclusion is further supported by galaxies that are predominantly atomic at all radii. Neither does this separation appear to be related to the surface mass density of NGC 628 becoming gas dominated. In Figure 7, we also indicate the stellar surface density determined from *Spitzer* 3.6 μm data by Querejeta et al. (2014) using the data from the S4G survey (Sheth et al. 2010), arbitrarily scaled by 0.1 to be on the same scale as the gas mass density. The disk of NGC 628 becomes gas dominated beyond the radius at which the IR deviates from $\Sigma_{\rm gas}$ (at $R_{25} \sim 1$).

The deviation of the submillimeter emission from the gas is more clearly seen in Figure 8, where we plot the ratio of mean gas-mass surface density to 500 μm surface brightness as a function of radius for NGC 628. At the inner radii of the galaxy, the $\Sigma_{\rm gas}/I_{500}$ ratio is flat and then increases in slope beyond $R_{25} \sim 0.7$. To demonstrate that this change is significant, we have shaded the data to indicate the fraction of pixels that are significant (S/N $>$ 3), with darker points indicating a larger fraction. This shading is conservative because we are integrating in annuli, meaning that we are more sensitive to diffuse emission at larger radii. Even given this conservative estimate, it is clear that the measured values of $\Sigma_{\rm gas}/I_{500}$ ratio are significant out to $R_{25} \sim 1$.

One possibility for this deviation is that we are seeing a change in the DGR at these radii, possibly related to a variation in the radial metallicity gradient at the larger radii. However, Moustakas et al. (2010) measure gas-phase abundances out to $\sim R_{25}$ for several of our galaxies, including NGC 628 (see their Figure 7), and no such changes in the abundance gradients are seen. The expected variation of the gas to dust ratio is indicated by the inverse of the metallicity gradient determined by Moustakas et al. (2010), using both the Kobulnicky & Kewley (2004) or Pilyugin & Thuan (2005) calibrations, as shown by the dashed and solid lines, respectively, on Figure 8. These lines are both normalized to the value of $\Sigma_{\rm gas}/I_{500}$ at $0.1 R_{25}$ to emphasize the similarity (or difference) of the determined metallicity slopes compared to the observed variation of the $\Sigma_{\rm gas}/I_{500}$ ratio. However, the lines also demonstrate the issues in interpreting the metallicity gradient. The Pilyugin & Thuan (2005) calibration follows reasonably well the observed $\Sigma_{\rm gas}/I_{500}$ ratio up to $R_{25} \sim 0.7$, beyond which a deviation from this slope is clearly visible. Though, the Kobulnicky & Kewley (2004) calibration shows a much steeper slope, and, while reasonable below $0.4 R_{25}$, over-estimates the observed ratio between 0.4 and

0.8 R_{25}, and no deviation of the Σ_{gas}/I_{500} ratio relative to this gradient is seen at larger radii. Which gradient is more representative of the true gas-phase abundance gradient is uncertain, however, Croxall et al. (2013) find a metallicity in between the two calibrations shown here at $R_{25} \sim 0.4$ using temperature insensitive metallicity calibration based on FIR fine-structure lines, suggesting that the gradient may lay between these lines.

The Σ_{gas}/I_{500} radial variations for the other galaxies in our sample are included in Figure 8. For all galaxies, this ratio lies between 20–30, with the ratio becoming larger at larger radii. Several galaxies also show a turn up in Σ_{gas}/I_{500} within $0.1R_{25}$, such as NGC 6946. The increase in the Σ_{gas}/I_{500} in these galaxy centers is likely associated with the decreased central α_{CO} values observed by Sandstrom et al. (2013) in several of our galaxies, including NGC 6946. A central decrease in α_{CO} would mean that we overestimate Σ_{gas} at the center of our galaxies due to our assumption of a constant Milky Way value, and hence overestimate the Σ_{gas}/I_{500} ratio. For galaxies for which it is available, we have also plotted the inverse of the determined metallicity gradients as in Figure 8. For several galaxies (e.g., NGC 3198) the metallicity gradient is sufficient to explain the observed radial trend in Σ_{gas}/I_{500}, with no significant deviations seen. For some galaxies, i.e., NGC 4254 and NGC 4321, the metallicity gradients are much steeper than the observed Σ_{gas}/I_{500} ratio. Given the observed gradients in gas- and stellar-surface-mass densities, it is possible that the metallicity gradients are much flatter than have been determined for these objects. Finally, for several galaxies, the same excess at large radii relative to the metallicity gradient as in NGC 628 is seen (e.g., NGC 925 and NGC 6946).

For these galaxiesms, which show a radial deviation in the Σ_{gas}/I_{500} ratio, such as NGC 628 and NGC 925, another possible explanation is that the different conditions in the outskirts of the galaxies lead to different dust properties, which result in different emissivities. Such a variation in the emissivity with radius for some of the KINGFISH galaxies has already been suggested by Galametz et al. (2014) using submillimeter data and in M33 by Tabatabaei et al. (2014).

However, at least some part of this deviation at large radii must arise from the decrease in the mean interstellar radiation field available to heat the dust at these radii, as demonstrated by the radial decrease in stellar density relative to gas density in Figure 7. A weaker interstellar radiation field will lead to lower average dust temperatures and thus correspondingly weaker IR emission. This can be seen in Figure 9, where we plot the same quantities as in Figure 7 for NGC 628, but now with the shorter wavelength SPIRE 250 μm band (note the different scaling factor). While it is clear in this figure that a change in the ratio of gas mass to IR luminosity occurs at a similar radius, the ratio decreases much more rapidly. This implies a change in the IR slope, and thus either a decrease in dust temperature or a flattening of the dust power-law emissivity. A decreasing dust temperature would lead to a lower IR luminosity even without a variation of the DGR.

In any case, it is clear from Figure 7 and the other galaxies that for the outskirts of many galaxies (beyond $\sim$0.7 R_{25}), the IR emission no longer traces the total gas mass in the same manner. For the galaxies in our sample, the total gas mass is dominated by the atomic gas at these radii. For many of our galaxies, a significant fraction of H I is found outside the optical radius (a median of 40% for our sample), and, for several objects, emission can be found even outside 2 R_{25}, with an obvious (and unrepresentative) example being NGC 3077 with its extended

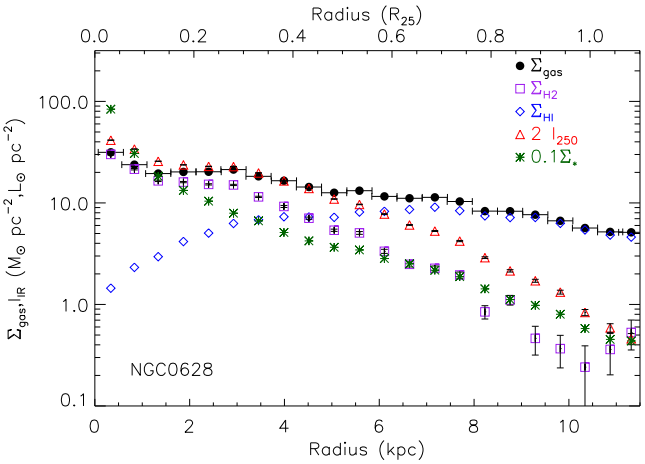

Figure 9. Same as Figure 7, but with the radial variation of the SPIRE 250 surface brightness in NGC 628. The SPIRE 250 surface brightness has been scaled by only two to place it on the same scale as the mass surface densities as it is closer to the peak of the IR SED. The HI, H_2, and total gas-mass surface densities are from Schruba et al. (2011).

tidal streams (Walter et al. 2011). By defining our apertures purely on the extent of the optical and IR emission, it is obvious that such extended gas disks will not be accounted for in the above relations, with the relations missing a large fraction of the total gas mass in some galaxies, like the H I-rich dwarfs like DDO154. However, it is still an open question how much relevance this extended H I gas has on the galaxy as a whole, with all of the molecular gas and most of the star formation inside our chosen "total" galaxy apertures and it being uncertain whether this gas external to the galaxy will participate at all in future star formation events within the galaxy.

5. SUMMARY

The evolution of the gas-mass density over cosmic time plays a direct role in the evolution of galaxies through its link to the SFR. Though, directly measuring the gas mass of a large number of galaxies at high redshifts through line observations is technically difficult and time consuming. As dust and gas are intimately associated, the dust infrared continuum may provide a more feasible way to determine the total gas mass of galaxies at high redshift. To demonstrate the use of the IR continuum as a gas tracer, we have compared the total gas mass and IR luminosity of a well-studied sample of 36 nearby galaxies (average distance 10 Mpc) observed with the KINGFISH, THINGS, and HERACLES surveys. These galaxies sample the peak of the mass function, with stellar masses from $\sim 10^{6.5}$ to $\sim 10^{10.5}\,M_{\odot}$, and, unlike the local merger-induced ULIRGs, these galaxies have disk-like morphologies that are likely more representative of the main-sequence galaxies at high redshift observed in current and future deep submillimeter surveys.

We find a strong correlation between the total gas mass and IR luminosity in all *Herschel* bands, with the strongest and tightest correlation found for the longest wavelength (SPIRE 500 μm). The gas to luminosity ratio, M_{gas}/L_{500}, is found to increase with decreasing submillimeter luminosity, which can be ascribed to the declining metallicity associated with the lower galaxy masses of the low luminosity galaxies. This declining metallicity will lead to a lower DGR, and therefore higher gas to dust luminosity ratio. We provide fits to the total gas mass versus IR luminosity relations for all *Herschel* bands, which

can be interpolated between to obtain an empirical relation to be used at any IR wavelength for determining the total gas mass (whose coefficients are given in Table 6). To minimize the effects of metallicity, we also fit only galaxies with stellar masses greater than $10^9\ M_\odot$ in our sample, which also results in a significantly reduced dispersion. For the SPIRE 500 band, we find that a linear relation is a reasonable approximation, and find that $\log(M_{\rm gas}/L_{500}) = 28.5\ [M_\odot/L_\odot]$, with a dispersion of only 0.118 dex.

The molecular gas-mass surface density has been demonstrated to be more tightly associated with the SFR than the atomic gas, thus we also provide calibrations for the molecular gas. We find similarly strong correlations, with the strongest correlation found for the PACS100 and PACS160 bands that lie at the peak of the IR emission, and are strongly correlated with the total IR luminosity. This correlation between L_{160} and $M_{\rm H2}$ appears to be driven mostly by the correlation of both the average dust temperature (as measured by PACS160/SPIRE 500) and molecular gas fraction ($L_{\rm CO}/M_{\rm gas}$) with galaxy mass and metallicity, with dwarf galaxies showing both warmer dust and lower molecular gas fractions. Given this correlation, we suggest that the L_{160}–$M_{\rm H2}$ relation not be applied to higher redshifts.

Using the resolved nature of the IR and gas surveys we employed in this survey, we also explored the correlations using elliptical annuli, and find the same correlations as the integrated comparisons, albeit with larger scatter. For most galaxies, we find that the $\Sigma_{\rm gas}/I_{500}$ ratio increases with radius, as expected from the determined radial metallicity gradients. However, for some galaxies the $\Sigma_{\rm gas}/I_{500}$ relation is observed to deviate from the metallicity gradient at larger radii, becoming much larger. A drop in the mean dust temperature plays at least some role in this observed excess, given the decrease in stellar mass surface densities relative to gas surface densities, and supported by the observed steeper $\Sigma_{\rm gas}$ to I_{250} relation relative to the I_{500} radial relation. This deviation in the $\Sigma_{\rm gas}/I_{500}$ ratio in the outskirts in galaxies, and the extended H I disks not visible in the IR observed in a fraction of our galaxies, suggest that the mass of extended gas in galaxies cannot be straightforwardly determined from the IR emission.

However, even with these radial trends, the total gas mass of galaxies within their optical radius can be well determined within a factor of two by observations of the submillimeter dust emission, and typically to within 30% for typical ($\log(M_*/M_\odot) > 9$) galaxies observed in high-redshift samples.

The authors thank the anonymous referee whose comments helped expand and improve the details of this work. The National Radio Astronomy Observatory is a facility of the National Science Foundation operated under cooperative agreement by Associated Universities, Inc.

REFERENCES

Abdalla, F. B., & Rawlings, S. 2005, MNRAS, 360, 27
Abdo, A. A., Ackermann, M., Ajello, M., et al. 2010, ApJ, 710, 133
Aniano, G., Draine, B. T., Calzetti, D., et al. 2012, ApJ, 756, 138
Auld, R., Bianchi, S., Smith, M. W. L., et al. 2013, MNRAS, 428, 1880
Barnes, D. G., Staveley-Smith, L., de Blok, W. J. G., et al. 2001, MNRAS, 322, 486
Bauermeister, A., Blitz, L., Bolatto, A., et al. 2013, ApJ, 768, 132
Bigiel, F., Leroy, A., Walter, F., et al. 2008, AJ, 136, 2846
Bolatto, A. D., Wolfire, M., & Leroy, A. K. 2013, ARA&A, 51, 207
Boquien, M., Boselli, A., Buat, V., et al. 2013, A&A, 554, A14
Boselli, A., Cortese, L., & Boquien, M. 2014a, A&A, 564, A65
Boselli, A., Cortese, L., Boquien, M., et al. 2014b, A&A, 564, A66
Boselli, A., Lequeux, J., & Gavazzi, G. 2002, A&A, 384, 33
Bourne, N., Dunne, L., Bendo, G. J., et al. 2013, MNRAS, 436, 479
Brinchmann, J., Charlot, S., White, S. D. M., et al. 2004, MNRAS, 351, 1151
Carilli, C. L., & Walter, F. 2013, ARA&A, 51, 105
Compiègne, M., Verstraete, L., Jones, A., et al. 2011, A&A, 525, A103
Corbelli, E., Bianchi, S., Cortese, L., et al. 2012, A&A, 542, A32
Croxall, K. V., Smith, J. D., Brandl, B. R., et al. 2013, ApJ, 777, 96
Dale, D. A., Aniano, G., Engelbracht, C. W., et al. 2012, ApJ, 745, 95
Decarli, R., Walter, F., Carilli, C., et al. 2014, ApJ, 782, 78
Draine, B. T., Dale, D. A., Bendo, G., et al. 2007, ApJ, 663, 866
Draine, B. T., & Li, A. 2007, ApJ, 657, 810
Duffy, A. R., Meyer, M. J., Staveley-Smith, L., et al. 2012, MNRAS, 426, 3385
Eales, S., Smith, M. W. L., Auld, R., et al. 2012, ApJ, 761, 168
Galametz, M., Albrecht, M., Kennicutt, R., et al. 2014, MNRAS, 439, 2542
Galliano, F., Hony, S., Bernard, J.-P., et al. 2011, A&A, 536, A88
Griffin, M. J., Abergel, A., Abreu, A., et al. 2010, A&A, 518, L3
Guelin, M., Zylka, R., Mezger, P. G., Haslam, C. G. T., & Kreysa, E. 1995, A&A, 298, L29
Guelin, M., Zylka, R., Mezger, P. G., et al. 1993, A&A, 279, L37
Haynes, M. P., Giovanelli, R., Martin, A. M., et al. 2011, AJ, 142, 170
Hildebrand, R. H. 1983, QJRAS, 24, 267
Hodge, J. A., Karim, A., Smail, I., et al. 2013, ApJ, 768, 91
Israel, F. P. 1997, A&A, 328, 471
Jenkins, E. B., & Savage, B. D. 1974, ApJ, 187, 243
Kainulainen, J., Alves, J., Beuther, H., Henning, T., & Schuller, F. 2011, A&A, 536, A48
Karim, A., Schinnerer, E., Martínez-Sansigre, A., et al. 2011, ApJ, 730, 61
Kennicutt, R. C., Jr. 1998, ApJ, 498, 541
Kennicutt, R. C., Jr., Armus, L., Bendo, G., et al. 2003, PASP, 115, 928
Kennicutt, R. C., Calzetti, D., Aniano, G., et al. 2011, PASP, 123, 1347
Kewley, L. J., & Ellison, S. L. 2008, ApJ, 681, 1183
Kobulnicky, H. A., & Kewley, L. J. 2004, ApJ, 617, 240
Kreckel, K., Groves, B., Schinnerer, E., et al. 2013, ApJ, 771, 62
Lada, C. J., Lada, E. A., Clemens, D. P., & Bally, J. 1994, ApJ, 429, 694
Leroy, A. K., Bolatto, A., Gordon, K., et al. 2011, ApJ, 737, 12
Leroy, A. K., Lee, C., Schruba, A., et al. 2013a, ApJL, 769, L12
Leroy, A. K., Walter, F., Bigiel, F., et al. 2009, AJ, 137, 4670
Leroy, A. K., Walter, F., Sandstrom, K., et al. 2013b, AJ, 146, 19
Madden, S. C., Galliano, F., Jones, A. P., & Sauvage, M. 2006, A&A, 446, 877
Magdis, G. E., Daddi, E., Béthermin, M., et al. 2012, ApJ, 760, 6
Magdis, G. E., Daddi, E., Elbaz, D., et al. 2011, ApJL, 740, L15
Magrini, L., Bianchi, S., Corbelli, E., et al. 2011, A&A, 535, A13
Meyer, M. 2009, Panoramic Radio Astronomy: Wide-field 1-2 GHz Research on Galaxy Evolution, http://pos.sissa.it/cgi-bin/reader/conf.cgi?confid=89
Moustakas, J., Kennicutt, R. C., Jr., Tremonti, C. A., et al. 2010, ApJS, 190, 233
Obreschkow, D., & Rawlings, S. 2009, ApJL, 696, L129
Pilbratt, G. L., Riedinger, J. R., Passvogel, T., et al. 2010, A&A, 518, L1
Pilyugin, L. S., & Thuan, T. X. 2005, ApJ, 631, 231
Poglitsch, A., Waelkens, C., Geis, N., et al. 2010, A&A, 518, L2
Prochaska, J. X., Herbert-Fort, S., & Wolfe, A. M. 2005, ApJ, 635, 123
Querejeta, M., Meidt, S. E., Schinnerer, E., et al. 2014, arXiv:1410.0009
Rémy-Ruyer, A., Madden, S. C., Galliano, F., et al. 2013, A&A, 557, A95
Rémy-Ruyer, A., Madden, S. C., Galliano, F., et al. 2014, A&A, 563, A31
Roussel, H. 2012, PASP, 125, 1126
Saintonge, A., Kauffmann, G., Kramer, C., et al. 2011a, MNRAS, 415, 32
Saintonge, A., Kauffmann, G., Wang, J., et al. 2011b, MNRAS, 415, 61
Sandstrom, K. M., Leroy, A. K., Walter, F., et al. 2013, ApJ, 777, 5
Santini, P., Maiolino, R., Magnelli, B., et al. 2014, A&A, 562, A30
Schruba, A., Leroy, A. K., Walter, F., et al. 2011, AJ, 142, 37
Scoville, N., Aussel, H., Sheth, K., et al. 2014, ApJ, 783, 84
Sheth, K., Regan, M., Hinz, J. L., et al. 2010, PASP, 122, 1397
Shetty, R., Kauffmann, J., Schnee, S., & Goodman, A. A. 2009, ApJ, 696, 676
Solomon, P. M., Rivolo, A. R., Barrett, J., & Yahil, A. 1987, ApJ, 319, 730
Solomon, P. M., & Vanden Bout, P. A. 2005, ARA&A, 43, 677
Smith, M. W. L., Gomez, H. L., Eales, S. A., et al. 2012, ApJ, 748, 123
Tabatabaei, F. S., Braine, J., Xilouris, E. M., et al. 2014, A&A, 561, A95
Tacconi, L. J., Neri, R., Genzel, R., et al. 2013, ApJ, 768, 74
Tremonti, C. A., Heckman, T. M., Kauffmann, G., et al. 2004, ApJ, 613, 898
Walter, F., Brinks, E., de Blok, W. J. G., et al. 2008, AJ, 136, 2563
Walter, F., Decarli, R., Sargent, M., et al. 2014, ApJ, 782, 79
Walter, F., Sandstrom, K., Aniano, G., et al. 2011, ApJL, 726, L11
Wolfire, M., Hollenbach, D., & McKee, C. 2010, ApJ, 716, 1191
Yabe, K., Ohta, K., Iwamuro, F., et al. 2014, MNRAS, 437, 3647
Young, J. S., Xie, S., Tacconi, L., et al. 1995, ApJS, 98, 219
Zubko, V., Dwek, E., & Arendt, R. G. 2004, ApJS, 152, 211